# Alternating *syn-anti* bacteriochlorophylls form concentric helical nanotubes in chlorosomes

Swapna Ganapathy[a], Gert T. Oostergetel[b], Piotr K. Wawrzyniak[a], Michael Reus[c], Aline Gomez Maqueo Chew[d,1], Francesco Buda[a], Egbert J. Boekema[b], Donald A. Bryant[d], Alfred R. Holzwarth[c], and Huub J. M. de Groot[a,2]

[a]Leiden Institute of Chemistry, P.O. Box 9502, 2300 RA Leiden, The Netherlands; [b]Groningen Biomolecular Sciences and Biotechnology Institute, 9747 AG Groningen, The Netherlands; [c]Max-Planck-Institut für Bioanorganische Chemie, D-45470 Mülheim an der Ruhr, Germany; and [d]Department of Biochemistry and Molecular Biology, The Pennsylvania State University, University Park, PA 16802

Communicated by Elisabeth Gantt, University of Maryland, College Park, MD, April 3, 2009 (received for review November 26, 2008)

**Chlorosomes are the largest and most efficient light-harvesting antennae found in nature, and they are constructed from hundreds of thousands of self-assembled bacteriochlorophyll (BChl) *c*, *d*, or *e* pigments. Because they form very large and compositionally heterogeneous organelles, they had been the only photosynthetic antenna system for which no detailed structural information was available. In our approach, the structure of a member of the chlorosome class was determined and compared with the wild type (WT) to resolve how the biological light-harvesting function of the chlorosome is established. By constructing a triple mutant, the heterogeneous BChl *c* pigment composition of chlorosomes of the green sulfur bacteria *Chlorobaculum tepidum* was simplified to nearly homogeneous BChl *d*. Computational integration of two different bioimaging techniques, solid-state NMR and cryoEM, revealed an undescribed *syn-anti* stacking mode and showed how ligated BChl *c* and *d* self-assemble into coaxial cylinders to form tubular-shaped elements. A close packing of BChls via $\pi$–$\pi$ stacking and helical H-bonding networks present in both the mutant and in the WT forms the basis for ultrafast, long-distance transmission of excitation energy. The structural framework is robust and can accommodate extensive chemical heterogeneity in the BChl side chains for adaptive optimization of the light-harvesting functionality in low-light environments. In addition, *syn-anti* BChl stacks form sheets that allow for strong exciton overlap in two dimensions enabling triplet exciton formation for efficient photoprotection.**

cryoEM | light-harvesting | photosynthesis | solid-state NMR | supramolecular aggregates

Chlorosomes are the principal light-harvesting apparatus of green sulfur bacteria, some green filamentous anoxygenic phototrophs, and the recently discovered aerobic anoxygenic phototroph *Candidatus* Chloracidobacterium thermophilum (1, 2). They are irregular, elongated sacs containing self-assembled BChls. They differ from other antenna complexes by their very large size (≈150 × 60 nm) and the absence of a protein matrix to support the photosynthetic pigments (1, 3, 4). Up to 250,000 BChls are organized into supramolecular light-harvesting devices with strongly red-shifted absorption bands and extremely large exciton diffusion lengths that cover up to 200 BChl monomers (5). Chlorosomes efficiently harvest light and are remarkably stable against photodegradation because of self-protection of the BChls from singlet oxygen (1, 6). They can form under extreme environmental conditions and allow for photosynthesis at extraordinarily low light intensities by ultrarapid transfer of energy into photosynthetic reaction centers (5, 7, 8). The unique optical and excitonic properties of chlorosomes are unknown for any other material, and chlorosomes may thus provide a basis for the rational design of biomimetic, self-assembling, and self-repairing structures for artificial photosynthesis and molecular electronics (9–11).

Chlorosomes are assembled from BChl *c*, *d*, or *e* and contain naturally heterogeneous molecular mixtures of BChls with different side chain modifications and stereochemistry (Fig. 1). In particular, chlorosomes of the green sulfur bacterium *Chlorobaculum tepidum* contain a complex mixture of BChl *c* molecules with variable degrees of methylation at carbons C-$8^2$ and C-$12^1$ (Fig. 1), variations in the esterifying alcohol side chain of the C-17 carboxyl group, and both *R*- and *S*-chirality at the C-$3^1$ carbon (1, 12). Because a heterogeneous structure cannot be determined by crystallographic methods, chlorosomes are the only class of antennae for which no structural information is currently available. Conflicting models have been derived from spectroscopic and electron microscopic assessments (13–16) and from studies with chemical analogs (17).

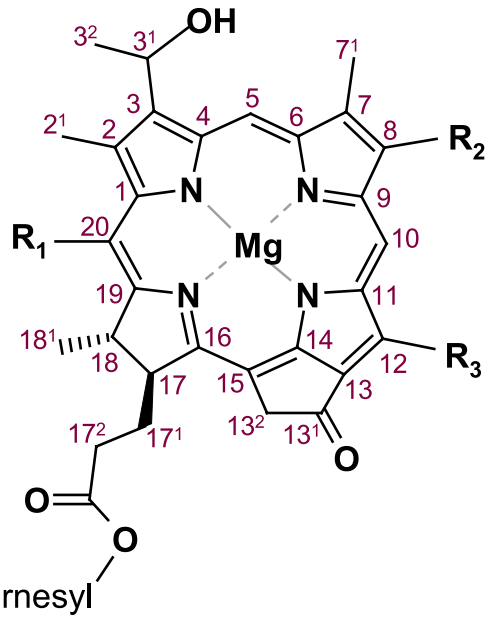


**Fig. 1.** BChl homologues for *C. tepidum*. In the WT, $R_1$ = Me; $R_2$ = Et, *n*-Pr, or *i*-Bu; $R_3$ = Me, or Et. In the *bchQRU* mutant $R_1$ = H; $R_2$ = Et; $R_3$ = Me.

Recent advances in understanding the biosynthesis of BChl *c* have led to a well-characterized *bchQ bchR bchU* (hereafter *bchQRU*) *C. tepidum* triple mutant (12). This mutant synthesizes well-defined, extended chlorosomes that contain >95% $17^2$-farnesyl-*R*-[8-ethyl,12-methyl]BChl *d* (Fig. 1) and form regularly packed, tubular-shaped elements with a diameter >10 nm that are interconnected via curved sheets (16, 18). The

Author contributions: E.J.B., A.R.H., D.A.B., and H.J.M.d.G. designed research; S.G., G.T.O., P.K.W., M.R., A.G.M.C., and F.B. performed research; S.G., G.T.O., P.K.W., and H.J.M.d.G. analyzed data; and S.G., D.A.B., and H.J.M.d.G. wrote the paper.

The authors declare no conflict of interest.

Freely available online through the PNAS open access option.

[1]Present address: Department of Microbiology, Ohio State University, Columbus, OH 43210.

[2]To whom correspondence should be addressed. E-mail: groot_h@lic.leidenuniv.nl.

This article contains supporting information online at www.pnas.org/cgi/content/full/0903534106/DCSupplemental.

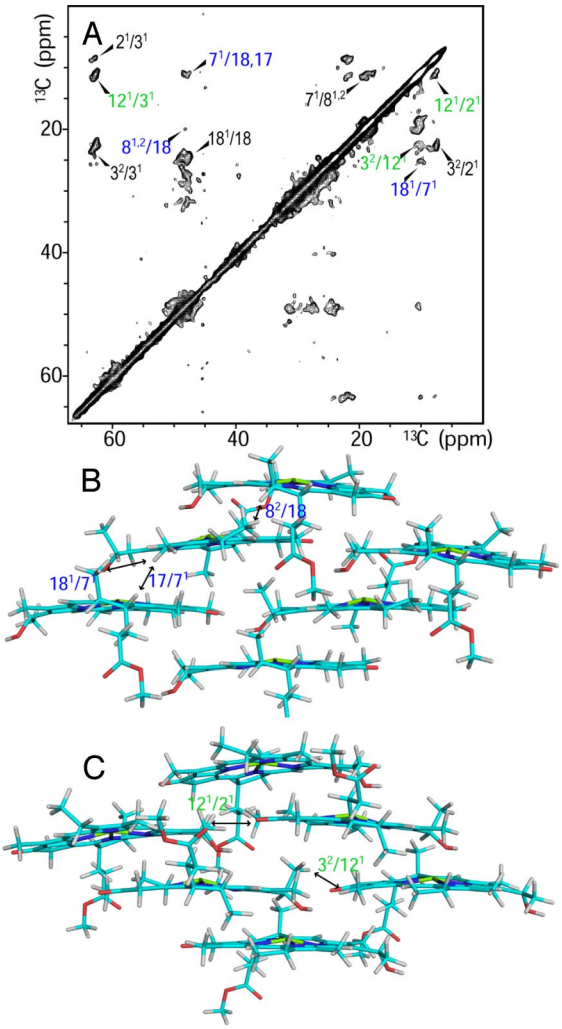


**Fig. 2.** Distance constraints from proton-mediated correlation spectroscopy. (*A*) $^{13}$C–$^{13}$C CHHC dataset of *bchQRU* chlorosomes, recorded at 17.6 T with 13 kHz spinning and 250 $\mu$s spin diffusion. Correlations labeled in blue are intermolecular intrastack, in green are intermolecular interstack, and black are intramolecular, respectively. (*B*) Two *syn-anti* stacks with three BChl *d* molecules each (farnesyl tails are replaced by methyl groups). The arrows indicate the side chains between which cross-peaks are seen. Intermolecular intrastack correlations are labeled. (*C*) View of *B* from the opposite side with the interstack cross-peaks indicated.

absence of a methyl group at C-20 and of side chain heterogeneity at C-8 and C-12, in combination with the very limited stereochemical heterogeneity at $3^1$ in the BChl *d* pigments of the chlorosomes from the *bchQRU* mutant, also provided very high-resolution magic-angle-spinning (MAS) solid-state NMR data that facilitated both the assignment of the spectra and the detection of distance constraints needed to determine the principal stacking mode and the arrangement of the BChls in periodic layers. When combined with cryoEM data that revealed a helical arrangement of chlorophyll stacks, this allowed the structure of the BChl arrangement within one member of the class of chlorosome antennae from the molecular to the supramolecular level to be solved. It was determined that pairs of alternating *syn-anti*-ligated BChl *d* stacks form sheets that self-assemble into coaxial tubes to support the efficient biological light-harvesting function by providing ultrafast helical exciton delocalization pathways along BChl stacks interconnected by hydrogen bonds.

**Table 1. List of intermolecular cross-peaks observed between the BChl *d* molecules of chlorosomes of the *bchQRU* mutant in the CHHC spectrum for a mixing time of 250 $\mu$s**

| CHHC contact | Shortest $^1$H–$^1$H distance, Å |
|---|---|
| $7^1/17$ | 2.32 |
| $7^1/18^1$ | 2.67 |
| $8^2/18$ | 1.84 |
| $2^1/12^1$ | 2.80 |
| $3^1/12^1$ | 2.64 |
| $3^2/12^1$ | 2.78 |

The corresponding shortest $^1$H–$^1$H distances taken from an optimized *syn-anti* stack aggregate of six stacks, each stack comprising 12 *syn-anti* coordinated BChl *d* molecules are listed. Optimization was done with molecular mechanics in Hyperchem 7.

## Results

The NMR assignments of the $^{13}$C and $^1$H signals of BChl *d* molecules in chlorosomes from the *bchQRU* mutant were obtained from 2D $^{13}$C–$^{13}$C and $^1$H–$^{13}$C magic-angle spinning (MAS), solid-state NMR dipolar correlation spectra [supporting information (SI) Figs. S1 and S2 and Tables S1 and S2] collected from $^{13}$C-enriched chlorosome preparations. The lines observed in $^{13}$C–$^{13}$C correlation datasets were very narrow, of the order of 1 ppm (Figs. S1 and S2). A $^{13}$C–$^{13}$C dataset recorded at a longer mixing time of 5.1 ms was needed to assign the farnesyl tail of BChl *d*, which meant that the tail is subject to restricted mobility. The assignments were made following previous NMR work on *C. tepidum* chlorosomes (15).

To proceed from the NMR chemical shift into the structure at the molecular level, proton-mediated correlation spectroscopy with a short mixing time of 250 $\mu$s was used (Fig. 2*A*) (19). Intermolecular correlations between BChl *d* molecules within a chlorosome were detected for $^1$H–$^1$H transfer events of $<$3 Å (Fig. 2*A* and Table 1). Because no intramolecular pathway that could serve to correlate the resonances over a 250-$\mu$s mixing time exists in the proton network, these correlations could be assigned unambiguously. The C-$7^1$/C-18, and C-$7^1$/C-$18^1$ intermolecular contacts (Fig. 2*B*) observed were especially significant because very few possibilities for molecular assembly exist in which these atoms can be in close proximity. The data revealed the presence of alternating monomers that form stacks assembled into layers with the farnesyl tails alternately extending on both sides. The two possible intermolecular arrangements that could satisfy these constraints are the new stacking model based on alternating *syn* and *anti* monomers (Fig. 3*D*) or antiparallel monomer stacking (Fig. 3*C*).

In addition to the intrastack correlations, intermolecular correlations between carbons C-$12^1$/C-$3^1$, C-$12^1$/C-$2^1$, and C-$12^1$/C-$3^2$ were detected between rings I and III of adjacent BChl *d* molecules. When *syn-anti* monomer stacks are combined to form a sheet, these distances are very short (Fig. 2*C* and Table 1), whereas for the antiparallel monomer stacking the shortest $^1$H–$^1$H distances between C-$12^1$/C-$3^1$, C-$12^1$/C-$2^1$, and C-$12^1$/C-$3^2$ are 3.46, 6.28, and 2.20 Å, respectively. Because the short mixing time of 250 $\mu$s produces $^1$H transfer over short distances $<$3 Å, the interstack correlations provide convincing evidence that *syn-anti* monomer stacking is the basic building block in the *bchQRU* chlorosome structure.

In chlorophyll aggregates, the $^1$H signals shift upfield by ring current effects from neighboring molecules (20). Density functional theory calculations were performed to estimate the ring currents for the *syn-anti* monomer model that was determined from the distance constraints, the antiparallel monomer model, and two earlier structural models that were proposed for BChl *c* in chlorosomes: the monomer-based, parallel-stack model (21) and the piggy-back dimer model (22) (Fig. 3). The *syn-anti* monomer stack has alter-

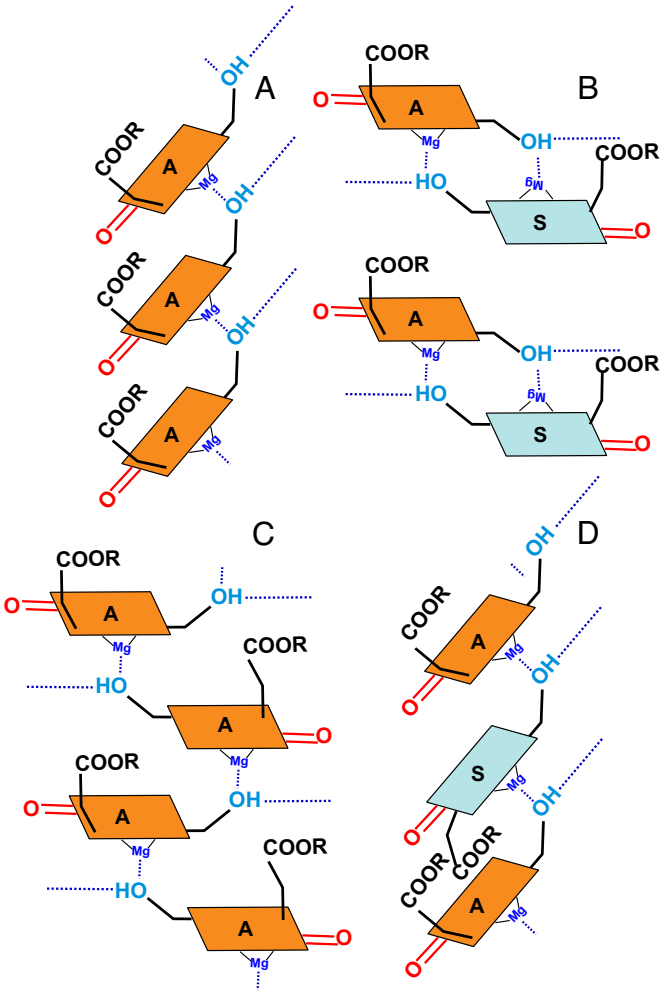


**Fig. 3.** Schematic representation of the four structural models used for the ring current shift calculations. (*A*) Parallel-stack model. (*B*) Piggy-back dimer model. (*C*) Antiparallel monomer stack model. (*D*) *Syn-anti* monomer stack model. A stack is defined as the structure for which one goes from one molecule of BChl to the next one via the O—Mg coordinate bond, then in the same molecule from the OH group again to the Mg of the next BChl molecule.

nating molecular conformations of the C-$3^1$ side chain, and *syn* or *anti* refers to the orientation of the OH ligation of adjacent BChls with respect to the farnesyl side chain. The calculated shifts for the antiparallel monomer stack model and the piggy-back dimer model are much larger than the experimentally observed shifts (see Table S1 and Fig. S3). These calculations showed that only the *syn-anti* monomer stack and the parallel stack can reproduce the experimental ring current shifts that are observed. In these two arrangements, each BChl *d* molecule has significant overlap with two adjacent molecules, via rings I and III, at opposite sides of the macroaromatic cycle (Fig. S4). The calculations for the piggy-back dimer model gave anomalously large proton ring current shifts at C-5–H, C-$3^1$–H, and C-$3^2$–$H_3$, whereas the antiparallel monomer stack gave a mismatch over the entire overlap region of C-1–C-5 and C-15–C-$13^2$. In these two arrangements, there is pronounced overlap with two neighbors at ring I, with correspondingly large ring current shifts, and little overlap at ring III, and this produces strongly asymmetric ring current shift patterns that were not observed experimentally (Fig. S4).

In end-on views of chlorosomes from the *bchQRU* mutant obtained with cryoEM, the BChls can be observed to form coaxial cylinders (Fig. 4*B*). In side views the concentric layers produce a regular pattern with a spacing of 2.10 ± 0.12 nm (Fig. 4 *A* and *D*) (16, 18). Additionally, a distinct, striped pattern with a spacing of 0.83 ± 0.01 nm was observed at a 90° angle to the layers (Fig. 4 *C* and *D*). After Fourier transformation, the layers translated into a single pair of equatorial reflections at 1/(2.1 nm) whereas the stripes gave rise to strong layer lines that revealed a predominant, helical arrangement with an axial repeat of 0.83 nm. In addition to the reflections from the 2.1-nm layer spacing, this spacing can clearly and reproducibly be observed in many images at high magnification.

To determine the arrangement of the BChl *d* molecules in the multilayer tubular structures of chlorosomes of the *bchQRU* mutant, supramolecular models were built for different orientations of the stacks relative to the tube axis (Figs. 4 and 5 and Fig. S5). With stacks running perpendicular to the tube axis along the circumference of a cylinder in rings, the simulated image and its Fourier transform reproduced the strong periodicity of 0.83 nm and the distinct striped appearance that is observed in the cryoEM images of the chlorosomes of the *bchQRU* mutant (compare Fig. 4 *C* and *E*). The 2.1-nm spacing is reproduced by combining several coaxial cylinders with an increment in the radius of 2.1 nm (Fig. 4 *E* and *F*). The high contrast of the structure in the chlorosomes of the *bchQRU* mutant arises from the orientation of the BChl molecular planes and the rotational symmetry (Fig. 5*B*). The plane of the molecules lies along the optical axis, i.e., the projection direction of the microscope, and the direction of the stacks lies along the circumference of the tubes. This organization leads to a strong alternation of high and low projected scattering density along the tube axis direction.

For the *C. tepidum* WT chlorosomes, the spacing between layers matches the separation of 2.1 nm observed in the chlorosomes of the *bchQRU* mutant (Fig. S5) (18). No other distinct spacing, similar to that in *bchQRU* mutant chlorosomes, could be detected visually in the cryoEM images. However, Fourier transforms of the images clearly showed the presence of a weak layerline at 1.22 ± 0.03 $nm^{-1}$ (Fig. S5). This periodicity corresponds to the distance between repeating *syn-anti* pair units in the direction of the stacks (Fig. 5 *A* and *C*), and the Fourier transform of the projected model structure shows a layer line at 1/1.25 $nm^{-1}$ (Fig. S5). Intermediate orientations of the stacks produced periodicities between 0.83 and 1.25 nm and failed to reproduce the characteristic cryoEM appearance of the chlorosomes of the *bchQRU* mutant or the WT.

In models in which the direction of the BChl stacks deviates slightly from the two orientations for WT and *bchQRU* mutant presented in Fig. 5, the expected spacing in the direction of the tube is insensitive to small variations around the 0 and 90° orientation of the stacks. Heterogeneity in the chlorosomes system generally will lead to partial symmetry breaking and a disappearance of the weaker layer lines while only the strongest one remains visible. For instance, in Fig. S5, for a model with stacks forming shallow helices instead of perfectly symmetric rings, only the layer line at 1/0.83 nm appears in the Fourier transform (Fig. S5), which is in agreement with Fourier transforms of the cryoEM images. Thus, stacks forming shallow left or right helices in *bchQRU* chlorosomes and stacks forming steeper helices in the WT chlorosomes are consistent with the EM data. In Fig. 5*A* the unit cell of the sheet is indicated, where $a$ = 1.25 nm is in the direction of the stack, and $b$ = 0.98 nm is at an angle of $\gamma = 122°$ to $a$. In Fig. 5*B* the basic helix is along the $b$-direction of the unit cell, with the stack perpendicular to the tube axis. For $n$ BChl pairs in each ring, the tube comprises a multistart helix with $n$-fold rotational symmetry (Fig. 5*B*). In contrast, the stacks in Fig. 5*C* do not form rings but lie along helices without rotational symmetry.

## Discussion

WT chlorosomes are much more heterogeneous than chlorosomes from the *bchQRU* mutant and contain BChl *c* molecules with a greater proportion of *S*-chirality at carbon C-$3^1$ and variable degrees of methylation at carbons C-$8^2$ and C-$12^1$.

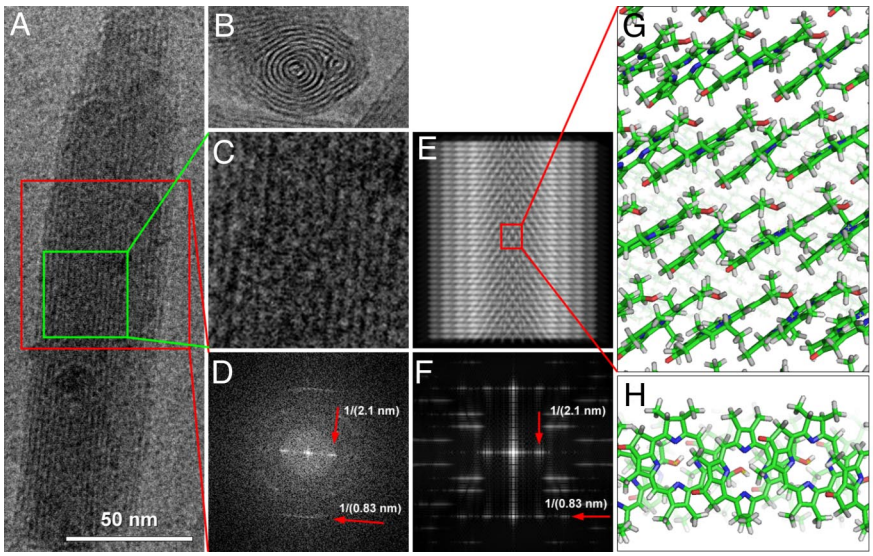


**Fig. 4.** Integration of cryoEM and NMR data to resolve the *bchQRU* mutant chlorosome structure. (*A* and *B*) CryoEM images of isolated chlorosomes from the *bchQRU* mutant of *C. tepidum* embedded in amorphous ice. A chlorosome is seen in side-on view (*A*) and in end-on view, showing the involuted layering of the BChls (*B*). (*C*) Enlarged region of the side-on view, indicated by the green box in *A*. (*D*) Fourier transform of the red-boxed region in *A*. The red arrows indicate reflections from a 2.1-nm spacing between BChl layers and a 0.83-nm spacing along the layers. (*E* and *F*) Simulated EM image and its Fourier transform, from a $17^2$-farnesyl-*R*-[8-ethyl,12-methyl]BChl *d* helical rod model comprising 4 tubes built from NMR-derived and geometry-optimized *syn-anti* monomer stacks that run along the circumference of the tubes, perpendicular to their long axis. The 1/0.83-nm periodicity corresponds to the spacing between adjacent BChl stacks running perpendicular to the tube axis. As explained in the text, there are no additional layer lines for shallow helices, and the blurring of the 2.1-nm reflections on the equator is because of disorder. (*G*) Enlarged view of the boxed area in *E*. (*H*) *Top* view, i.e., along the tube axis.

Additionally, end views of WT chlorosomes by cryoEM had shown that the internal organization of BChls was unique in individual chlorosomes (18). This extensive heterogeneity had thus far prevented a precise determination of the structure at the molecular level. However, the chlorosomes of the *bchQRU* mutant provided the possibility for understanding the underpinning of the chlorosome suprastructure, optical properties, and variability among species.

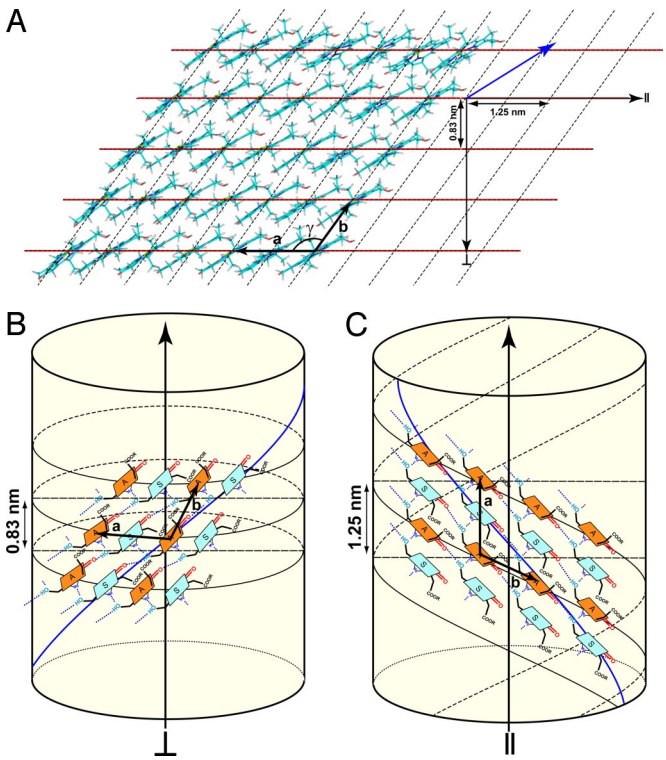


**Fig. 5.** Structural models of chlorosomes in the *bchQRU* mutant and the WT. (*A*) 7 × 5 section of the *syn-anti* array. The stacks are indicated by red lines. The separation perpendicular (⊥) to the stacks is 0.83 nm. The unit cell dimensions are: $a = 1.25$, $b = 0.98$, $\gamma = 122°$. The repeat in the direction parallel (∥) to the stack is 1.25 nm. (*B* and *C*) Multistart helices with the long axis running perpendicular or parallel to the stacks. Periodicities of 1.25 nm and 0.83 nm are indicated. The *syn-anti* pairs in *B* form a multistart helix with rotational symmetry. The H-bond helices that connect BChl stacks via the carbonyls are shown in blue and are right-handed in *B* and left-handed in *C*.

The two supramolecular arrangements, with stacks running parallel or perpendicular to the tube axis, produce similar O—H···O═C exciton delocalization pathways. Both for *syn-anti* monomer stacks running perpendicular and for stacks parallel to the tube axis, the monomer transition moments align along the H-bond network to form helices along the concentric tube walls (Fig. 5 *B* and *C*). The optical transition dipole moment for the monomer runs through the C-$13^1$ carbonyl group, along the hydrogen bonds. After excitation, the excitons would move through the BChl aggregates along helical trajectories following the O—H···O═C connection pathway, which reflects the macroscopic chirality of the system (8). When tubes are formed by bending the molecular arrays in the opposite direction, the helicities also change sign. The bending direction will thus affect the circular dichroism sign, which has often been reported to vary in different preparations (23). The inclination of the optical transition dipole moment of the monomers with respect to the long axis of the tube in Fig. 5*B* is ≈55°. The structural arrangement of the BChls in sheets with overlap between the stacks allows for strong triplet–triplet exciton interactions, which forms the basis for the self-protection of the chlorosome against photodegradation in high light under oxic conditions (6).

Chlorosomes were probably an early invention in biology because they are found in three of the six groups of chlorophototrophs, and two of those three groups have homodimeric type 1 reaction centers (1, 2). The self-organization of the BChls into layers spaced by 2.1 nm is a common property that is preserved across species and allows for the inclusion of carotenoids and quinones by packing between the esterifying alcohols of the chlorins (18). The concentric tube structure of chlorosomes is optimal for very efficient energy transfer in a very large antenna, a prerequisite for photosynthetic growth under very weak light conditions. The suprastructure is stabilized by the underlying principles of the self-assembly process, whereas its size and heterogeneity can be optimized for optimal functionality. As measured by the growth rate of cells, the larger, more complex and heterogeneous WT chlorosomes outperform the chlorosomes of the *bchQRU* mutant at all light intensities between 5 and 200 $\mu$mol of photons $m^{-2}$ $s^{-1}$ (12). Consistent with the idea that BChl *c* in a larger number of environments leads to better light harvesting, the half-band width of the $Q_y$ absorption maximum of the BChl *c* aggregates is largest for WT chlorosomes isolated from cells grown at low light intensity and is also much broader than for chlorosomes of the *bchQRU* mutant (12). When grown at very low

light intensity (≈5 μmol of photons $m^{-2}$ $s^{-1}$), *C. tepidum* cells produce approximately three times more BChl *c* than cells grown at high light intensity (>100 μmol of photons $m^{-2}$ $s^{-1}$). Because the cell size does not change and the number of chlorosomes per cell does not change dramatically, the number of BChls per chlorosome must increase by ≈3-fold (12).

Because the electronic properties of the supramolecular system and the absorption cross-section of the antenna can be modified by introducing disorder at the molecular level, functional advantages are achieved by adopting a suprastructure that is sufficiently plastic and flexible to accommodate considerable chemical heterogeneity. In the modeling, the two configurations having stacks running parallel or perpendicular to the tube axis correspond to local minima in the energy landscape of the suprastructure that permit chemical heterogeneity to be embedded within the structure. The layer lines observed in the Fourier transforms of the cryoEM data from the WT reveal extended periodic regions of stacks built from BChl pairs that run parallel to the tube axis in the suprastructure (Fig. 5*C*). Hence, the suprastructure is sufficiently stable to accept BChl *c* with methyl or ethyl side chains at C-12 and ethyl, propyl, or isobutyl side chains at C-8 of the tetrapyrrole ring. Likewise, the suprastructure must accommodate the variable amounts of BChls with *R*- and *S*-chirality at C-$3^1$ that the WT organism normally produces. This provides a window for evolutionary optimization through natural selection by diversification in the BChl side chains by coupling the replication/reproduction machinery (i.e., the growth rate) to the biosynthesis of the chlorophylls.

To couple non-protein-based light harvesting to gene evolution required the optimization of BChls and chlorosomes with respect to the predominant environmental constraint, low light intensity. Unmodified [8-ethyl,12-methyl]BChl *d*, found in the *bchQRU* mutant, with absorption similar to Chl *d*, is the easiest of the compounds to synthesize, requiring only three steps beyond chlorophyllide (12). However, its more regular, self-assembled structure has suboptimal optical properties. With essentially only $17^2$-farnesyl-[8-ethyl,12-methyl]BChl *d* the organism produces chlorosomes with very large BChl exciton domains and few nanotubes per chlorosome. The absorption spectrum is much narrower and is shifted to the blue by ≈15 nm compared with the WT, which still leaves significant overlap with the absorption of Chl *a* that is typically found in the overlying oxygenic aerobic chlorophototrophs (12). Three additional biosynthetic steps (six in total) are required beyond chlorophyllide to synthesize natural BChl *c*, and this probably has biological significance. The methylations at C-8 and C-12 in the WT contribute to tuning the wavelength of the $Q_y$ absorption maximum and to increasing the absorption cross-section by inhomogeneous broadening because of the many different microenvironments of the BChls (12). In addition, *C. tepidum* synthesizes a higher proportion of BChls with *S*-chirality at C-$3^1$ at low light intensity (24), and this may produce a larger number of "BChl domains" per chlorosome as well as smaller "domains" as marked by edges. The robust structural framework allows the organism to avoid producing arrays with larger and larger numbers of BChl *c* at decreasing light intensity. A very large increase in the domain size of the antenna would probably reduce the energy transfer efficiency to the baseplate BChl *a* ($B_{790}$), to the BChl *a*-binding Fenna–Matthews–Olson protein, and ultimately to the reaction centers.

Finally, the scaffolding according to Figs. 4 and 5 confirms that the structure of the chlorosome is established by self-assembly driven by noncovalent interactions without requiring proteins to provide coordinating ligands and structural control of BChl positioning. These interactions are (*i*) coordination of the C-$3^1$-hydroxyl to the magnesium ion, (*ii*) hydrogen bonding between the C-$3^1$-hydroxyl to the C-$13^1$-keto group, (*iii*) $\pi$–$\pi$ stacking between the extended chlorin chromophores (20), (*iv*) electrostatic interactions, and (*v*) partitioning of aliphatic tails into the hydrophobic parts of the suprastructure. In particular the polarized keto group with negative charge on oxygen interacts electrostatically with the $Mg^{2+}$, which is considered the most important electrostatic contribution to the aggregation (2). Because it does not involve any direct binding of the keto moiety to the metal, it contributes to strengthening the hydrogen bond, in contrast to inferences from chemical modeling studies (5).

In conclusion, researchers have debated for decades about the structure of the chlorosome, which consists of hundreds of thousands of BChls self-assembled into the most efficient light-harvesting antennae in nature. By genetic modification of the BChl biosynthesis pathway, the inherent disorder in the chlorosomes of *C. tepidum* was reduced without functionally disturbing the self-assembly process. Computational integration of cryoEM and solid-state NMR was used in this work to extend and connect the structure information from the molecular to the supramolecular level for the *bchQRU* mutant to obtain very detailed structure information. This method may well prove useful in the future for the solution of other biological structures that cannot be crystallized or are inherently disordered. The mutant structure provides a template for the evaluation of the more complex structure of the WT. Both chlorosome suprastructures are built from *syn-anti* monomer stacks self-assembled into nanotubes. The basis for the efficient and ultrafast light harvesting is a helical exciton delocalization pathway that is realized with stacks running parallel or perpendicular to the tube axis in WT and mutant, respectively. The suprastructure can accommodate heterogeneity in the side chains for evolutionary optimization of light harvesting without the direct intervention of proteins to scaffold the pigment molecules. This latter feature must have been critical to the evolution of these structures in natural environments that are severely energy limited.

## Materials and Methods

**Sample Preparation.** Cells of the *C. tepidum bchQRU* triple mutant strain described by Gomez Maqueo Chew et al. (12) were grown as described by Balaban et al. (14). Samples of the corresponding WT strain were also prepared for comparison. Cultures were grown in 1.5-L fermentation bottles with continuous slow stirring at 40 °C. Growth light was controlled at the surface of the bottles (25 μE $m^{-2}$ $s^{-1}$ photosynthetically active radiation) provided by two 40-W fluorescent neon tubes. For the *bchQRU* mutant and the WT, cells uniformly labeled with $^{13}C$ were obtained in steps. First, a 50-mL inoculum of cells grown in Wahlund medium was inoculated into Wahlund medium without acetate (1 L). In the next step, a 50-mL cell inoculum obtained from the acetate-free culture was inoculated into Wahlund medium (1 L) containing sodium [$^{13}C$]bicarbonate as the sole carbon source. Cells were grown for 3 days and then harvested by centrifugation. Chlorosomes from the two cell types, with the BChl *a*-containing baseplate attached, were isolated as described in ref. 14. Membranes were incubated for 1 h with 0.7% (wt/vol) lauryl dimethylamine oxide (LDAO) at an $OD_{max}$ = 20 $cm^{-1}$ at the wavelength of maximum absorbance in the $Q_y$ region between 700 and 750 nm. Chlorosomes were isolated by sucrose density gradient centrifugation; the gradients had a bottom layer of 50% (wt/vol) sucrose and a linear gradient from 10 to 40% (wt/vol) sucrose. The collected chlorosome band was diluted in 20 mM Tris·HCl (pH 8.0) to bring the sample below the critical micellar concentration (≈1–2 mM) of LDAO. The sample was washed to remove sucrose and LDAO by ultrafiltration in an Amicon concentrator equipped with a YM-100 membrane. The final chlorosome suspensions in Tris·HCl buffer showed the expected visible absorption maxima. Chlorosomes were kept in the dark at ≈4 °C before EM and NMR data collection. The pigments from the chlorosomes of the *bchQRU* mutant were also isolated and analyzed following the methods described in Steensgaard et al. (25), and >95% of $17^2$-farnesyl-*R*-[8-ethyl,12-methyl]BChl *d* was found. For the EM, chlorosomes were also prepared with the NaSCN method (26). To facilitate the freezing process for EM, the 2 M NaSCN was removed by dialysis against buffer. The tendency of chlorosomes to clump together was much less with the NaSCN than for the LDAO preparation, which facilitated the EM measurements.

**NMR Measurements.** All solid-state, MAS NMR experiments were performed with a Bruker AV-750 spectrometer equipped with a 4-mm triple resonance MAS probe head (Bruker) by using a $^{13}C$ radio frequency of 188.6 MHz and a sample temperature of 277 K. Spinning frequencies of 11 kHz ± 5 Hz and 13 kHz ± 5 Hz were used for 2D $^{13}C$–$^{13}C$ homo- and $^1H$–$^{13}C$ heteronuclear correlation experiments, respectively. The $^1H$ spins were decoupled during acquisition by using the two-pulse phase modulation scheme (27) in all of the experiments. Two-dimensional $^{13}C$–$^{13}C$ dipolar correlation spectra were recorded by using the radio

frequency-driven, dipolar recoupling sequence (28) with phase-sensitive detection in $\omega_1$ at mixing times of 1.4 ms (Fig. S1), 2.9 ms (Fig. S2), and 5.1 ms. A $^1$H $\pi/2$ pulse length of 3.1 $\mu$s was used with cross-polarization periods of 2 ms. For each of the 256 steps in the indirect dimension, 128 scans were collected. Two-dimensional $^{13}$C–$^{13}$C spectra were recorded by using the CHHC/CP$^3$ sequence (19, 29) for indirect detection of $^1$H–$^1$H contacts at $^1$H diffusion times of 250 $\mu$s (Fig. 2*A*) and 325 $\mu$s. The initial CP contact time was set to 256 $\mu$s. Short CP contact times of 128 $\mu$s enclosing the $^1$H–$^1$H spin diffusion step were used to ensure that the polarization transfer was restricted to directly bonded $^1$H–$^{13}$C spin pairs. For each of the 256 steps in the indirect dimension, 128 scans were collected. Two-dimensional $^1$H–$^{13}$C heteronuclear correlation data were collected by using the frequency-switched Lee–Goldburg (FSLG) experiment (30), with a short CP time of 256 $\mu$s and a $^1$H 90° pulse of 3.1 $\mu$s (Fig. S1). The $^1$H chemical shift scale was calibrated from a FSLG spectrum of solid tyrosine·HCl salt and validated with the chemical shift correlation plots (Fig. S6). For each of the 128 steps in the indirect $^1$H dimension, 128 $^{13}$C scans were accumulated.

**CryoEM Measurements.** Aliquots of purified chlorosomes were applied to holey carbon grids with a thin layer of carbon and were plunge-frozen in liquid ethane at 83 K with a Vitrobot vitrification system (FEI). Electron microscopy was performed with a Tecnai G2 Polara electron microscope (FEI) equipped with a Gatan energy filter at 115,000× magnification and a specimen temperature of 80 K. Images were recorded in the zero-loss imaging mode, by using a slit-width of 20 eV, with a slow-scan CCD camera at 1 $\mu$m underfocus, to have optimal phase contrast transfer at 300 kV for details with a periodicity of ≈2 nm. Rotational averaging of EM data revealed concentric tubes (Fig. S7). EM images were simulated as projected electron density from atomic coordinates at 0.6-nm resolution by using the EMAN pdb2mrc program (31) (Fig. 2).

**Structure Modeling and Ring Current Calculation.** A larger section of the *syn-anti* structure comprising of six stacks with 12 interacting BChl *d* molecules each was optimized in the computer by using an MM+ force field with a Polak–Ribiere conjugate gradient algorithm and with a gradient convergence criterion of 0.01 kcal/mol in Hyperchem 7. A *syn-anti* pair taken from this optimized structure was used to construct the larger multilayer tubular structures. From these atomic models, the electron density was calculated and projected down to create side views at a resolution of 0.6 nm for comparison with the experimental cryoEM data. In this way a composite image is produced by integration of the constraints obtained by the two methods, cryoEM and NMR, which can be visually compared with the biological specimen (Fig. 4). Density functional theory calculations were performed by using the Gaussian 03 software package (32) and the Becke, Lee, Yang, and Parr (BLYP) (33, 34) exchange-correlation functional, which has been used before to estimate NMR shifts for Chl systems (35). The 6–311++G(d,p) Gaussian basis set was used. To calculate the magnetic shielding caused by the local magnetic field induced by the ring current effect in the BChls, nucleus-independent chemical shift quantum mechanical calculations were performed (36). Ring current shifts were calculated by using the gauge-independent atomic orbital method (37–39).

**ACKNOWLEDGMENTS.** We thank I. de Boer, C. Erkelens, A. Lefeber, and J. Hollander for their assistance. This work was supported by Netherlands Organization for Scientific Research-Division of Chemical Sciences, the Volkswagen Stiftung, and U. S. Department of Energy Grant DE-FG02-94ER20137 (to D.A.B.).

1. Frigaard NU, Bryant DA (2006) in *Microbiology Monographs*, ed. Shively JM (Springer, Berlin), Vol 2, pp 79–114.
2. Bryant DA, et al. (2007) *Candidatus Chloracidobacterium thermophilum*: An aerobic phototrophic acidobacterium. *Science* 317:523–526.
3. Frigaard NU, Li H, Milks KJ, Bryant DA (2004) Nine mutants of *Chlorobium tepidum* each unable to synthesize a different chlorosome protein still assemble functional chlorosomes. *J Bacteriol* 186:646–653.
4. Holzwarth AR, Griebenow K, Schaffner K (1990) A photosynthetic antenna system which contains a protein-free chromophore aggregate. *Z Naturforsch C* 45:203–206.
5. Prokhorenko VI, et al. (2002) Energy transfer in supramolecular artificial antennae units of synthetic zinc chlorins and coaggregated energy traps: A time-resolved fluorescence study *J Phys Chem B* 106:5761–5768.
6. Kim H, et al. (2007) Triplet exciton formation as a novel photoprotection mechanism in chlorosomes of *Chlorobium tepidum*. *Biophys J* 93:192–201.
7. Holzwarth AR, Müller MG, Griebenow K (1990) Picosecond energy transfer kinetics between pigment pools in different preparations of chlorosomes from the green bacterium *Chloroflexus aurantiacus* ok-70-fl. *J Photochem Photobiol B* 5:457–465.
8. Prokhorenko VI, Steensgaard DB, Holzwarth AR (2003) Exciton theory for supramolecular chlorosomal aggregates. 1. Aggregate size dependence of the linear spectra. *Biophys J* 85:3173–3186.
9. Tamiaki H, Holzwarth AR, Schaffner K (1992) A synthetic zinc chlorin aggregate as a model for the supramolecular antenna complexes in the chlorosomes of green bacteria. *J Photochem Photobiol B* 15:355–360.
10. Huber V, Lysetska M, Würthner F (2007) Self-assembled single- and double-stack $\pi$-aggregates of chlorophyll derivatives on highly ordered pyrolytic graphite. *Small* 3:1007–1014.
11. Schenning APHJ, Meijer EW (2005) Supramolecular electronics: Nanowires from self-assembled $\pi$-conjugated systems. *Chem Commun* 26:3245–3258.
12. Gomez Maqueo Chew A, Frigaard NU, Bryant DA (2007) Bacteriochlorophyllide *c* C-8$^2$ and C-12$^1$ methyltransferases are essential for adaptation to low light in *Chlorobaculum tepidum*. *J Bacteriol* 189:6176–6184.
13. Nozawa T, et al. (1994) Structures of chlorosomes and aggregated BChl *c* in *Chlorobium tepidum* from solid-state high-resolution CP-MAS $^{13}$C NMR. *Photosynth Res* 41:211–223.
14. Balaban TS, et al. (1995) CP-MAS $^{13}$C-NMR dipolar correlation spectroscopy of $^{13}$C-enriched chlorosomes and isolated bacteriochlorophyll-*c* aggregates of *Chlorobium tepidum*: *The* self-organization of pigments is the main structural feature of chlorosomes. *Biochemistry* 34:15259–15266.
15. van Rossum BJ, et al. (2001) A refined model of the chlorosomal antennae of the green bacterium *Chlorobium tepidum* from proton chemical shift constraints obtained with high-field 2D and 3D MAS NMR dipolar correlation spectroscopy. *Biochemistry* 40:1587–1595.
16. Psencik J, et al. (2004) Lamellar organization of pigments in chlorosomes, the light harvesting complexes of green photosynthetic bacteria. *Biophys J* 87:1165–1172.
17. Jochum T, et al. (2008) The supramolecular organization of self-assembling chlorosomal bacteriochlorophyll *c*, *d*, or *e* mimics. *Proc Natl Acad Sci USA* 105:12736–12741.
18. Oostergetel GT, et al. (2007) Long-range organization of bacteriochlorophyll in chlorosomes of *Chlorobium tepidum* investigated by cryoelectron microscopy. *FEBS Lett* 581:5435–5439.
19. de Boer I, et al. (2002) 2D $^{13}$C–$^{13}$C MAS NMR correlation spectroscopy with mixing by true $^1$H spin diffusion reveals long-range intermolecular distance restraints in ultra high magnetic field. *J Magn Reson* 157:286–291.
20. Abraham RJ, Rowan AE (1991) in *Chlorophylls*, ed Scheer H (CRC, Boca Raton, FL), pp 797–834.
21. Holzwarth AR, Schaffner K (1994) On the structure of bacteriochlorophyll molecular aggregates in the chlorosomes of green bacteria: A molecular modeling study. *Photosynth Res* 41:225–233.
22. Egawa A, et al. (2007) Structure of the light-harvesting bacteriochlorophyll *c* assembly in chlorosomes from *Chlorobium limicola* determined by solid-state NMR. *Proc Natl Acad Sci USA* 104:790–795.
23. Griebenow K, Holzwarth AR, van Mourik F, van Grondelle R (1991) Pigment organization and energy transfer in green bacteria. 2. Circular and linear dichroism spectra of protein-containing and protein-free chlorosomes isolated from *Chloroflexus aurantiacus* strain Ok-70-Fl. *Biochim Biophys Acta* 1058:194–202.
24. Ishii T, et al. (2000) The effects of epimerization at the 3$^1$-position of bacteriochlorophylls *c* on their aggregation in chlorosomes of green sulfur bacteria. Control of the ratio of 3$^1$ epimers by light intensity. *Photochem Photobiol* 71:567–573.
25. Steensgaard DB, Wackerbarth H, Hildebrandt P, Holzwarth AR (2000) Diastereoselective control of bacteriochlorophyll *e* aggregation. 3$^1$-S-BChl *e* is essential for the formation of chlorosome-like aggregates. *J Phys Chem B* 104:10379–10386.
26. Gerola PD, Olson JM (1986) A new bacteriochlorophyll alpha-protein complex associated with chlorosomes of green sulfur bacteria. *Biochim Biophys Acta* 848:69–76.
27. Bennett AE, et al. (1995) Heteronuclear decoupling in rotating solids. *J Chem Phys* 103:6951–6958.
28. Bennett AE, Ok JH, Griffin RG, Vega S (1992) Chemical-shift correlation spectroscopy in rotating solids: Radio frequency-driven dipolar recoupling and longitudinal exchange. *J Chem Phys* 96:8624–8627.
29. Lange A, Luca S, Baldus M (2002) Structural constraints from proton-mediated rare-spin correlation spectroscopy in rotating solids. *J Am Chem Soc* 124:9704–9705.
30. van Rossum BJ, Förster H, de Groot HJM (1997) High-field and high-speed CP-MAS $^{13}$C NMR heteronuclear dipolar-correlation spectroscopy of solids with frequency-switched *Lee–Goldburg* homonuclear decoupling. *J Magn Reson* 124:516–519.
31. Ludtke SJ, Baldwin PR, Chiu W (1999) EMAN: Semiautomated software for high-resolution single-particle reconstructions. *J Struct Biol* 128:82–97.
32. Frisch MJ, et al. (2004) Gaussian 03, Revision D.01. (Gaussian, Wallingford CT).
33. Becke AD (1986) Density functional calculations of molecular bond energies. *J Chem Phys* 84:4524–4529.
34. Lee CT, Yang WT, Parr RG (1988) Development of the Colle–Salvetti correlation-energy formula into a functional of the electron density. *Phys Rev B* 37:785–789.
35. Facelli JC (1998) Density functional theory calculations of the structure and the $^{15}$N and $^{13}$C chemical shifts of methyl bacteriopheophorbide *a* and bacteriochlorophyll *a*. *J Phys Chem B* 102:2111–2116.
36. Chen ZF, et al. (2005) Nucleus-independent chemical shifts (NICS) as an aromaticity criterion. *Chem Rev* 105:3842–3888.
37. Ditchfield R (1972) Molecular orbital theory of magnetic shielding and magnetic susceptibility. *J Chem Phys* 56:5688–5691.
38. Ditchfield R (1974) Self-consistent perturbation theory of diamagnetism. 1. Gauge-invariant LCAO method for NMR chemical shifts. *Mol Phys* 27:789–807.
39. Wolinski K, Hinton JF, Pulay P (1990) Efficient implementation of the gauge-independent atomic orbital method for chemical shift calculations. *J Am Chem Soc* 112:8251–8260.